Catalysis Science & Technology

Accepted Manuscript

This article can be cited before page numbers have been issued, to do this please use: A. Alex, S. D. Adhikari, H. Kumar and S. Choudhury, *Catal. Sci. Technol.*, 2026, DOI: 10.1039/D6CY00235H.

ROYAL SOCIETY OF CHEMISTRY

rsc.li/catalysis

View Article Online
DOI: 10.1039/D6CY00235H

ARTICLE

Accelerated Synthesis of Inversely Vulcanized Polymers with Oligoethylene Unit Bearing Comonomer for Lithium–Sulfur Battery Application

Received 00th January 20xx,
Accepted 00th January 20xx

DOI: 10.1039/x0xx00000x

Aby Alex,[a] Soumyashree Das Adhikari,[b] Hemant Kumar,[b] Soumyadip Choudhury,[a,c*]

Lithium–sulfur (Li–S) batteries are considered a promising next-generation energy storage technology owing to their high theoretical capacity (1675 mAh·g^{-1}) and low cost. However, their practical deployment is hindered by the polysulfide shuttle effect and rapid capacity fading. Inverse vulcanization has emerged as an effective strategy to obtain sulfur-rich polymers that mimic the redox activity of elemental sulfur, yet many comonomers are excluded due to low boiling points or polarity mismatches, leading to premature homopolymerization or phase separation. This work overcomes these limitations through catalytic inverse vulcanization, producing polysulfidic copolymers bearing oligoethylene segments by reacting sulfur with triethyleneglycol dimethacrylate (TEGDMA) using zinc diethyldithiocarbamate (ZDEC) as a catalyst, commonly regarded as vulcanization accelerators. Spectroscopic and thermal analyses (FT-IR, Raman, XPS, XRD, DSC, TGA) confirm successful copolymer formation. Theoretical studies further show that the ZDEC activates sulfur, promoting efficient polymerization with TEGDMA. The resulting sulfur-rich copolymer is used as cathode active material in Li–S batteries, with multi-walled carbon nanotubes (MWCNTs) serving as a porous conductive host. SEM, TEM, and EDAX analyses reveal uniform dispersion and a sulfur-rich surface. Electrochemical testing demonstrates high initial capacity (1182.2 mAh·g^{-1} at 0.1C), effective utilization of active material, stability over 100 cycles, and striking rate performance compared to conventional sulfur cathodes.

1. Introduction

Lithium-sulfur (Li-S) batteries have emerged as a promising next-generation energy storage technology, offering the potential to overcome the limitations of conventional lithium-ion batteries (LIBs).[1] Although the LIB technology, historically and presently the dominant element in portable devices, is gradually approaching theoretical limitations in terms of energy density, thus hindering device performance despite all sorts of recent progress in LIBs. Thus, the development and investigation of next-generation lightweight, cost-effective batteries with high energy density represent an urgent, ongoing research target worldwide. To meet the high energy demand of the future, we require energy storage devices with an energy density exceeding 500 Wh·kg^{-1}.[2] With the increasing demand globally for high-energy-density storage systems to power electric vehicles (EVs), portable electronics, and renewable energy grids, Li-S batteries have garnered significant attention due to their exceptional theoretical energy density (~2600 Wh·kg^{-1}), which is far superior to that of traditional LIBs.[3,4] This is primarily attributed to the high specific capacity (1675 mAh·g^{-1}) and the lightweight nature of sulfur and lithium.[5] The high specific capacity stems from the conversion of sulfur to lithium sulfide (Li_2S), which involves the reversible transfer of 2 electrons per sulfur atom during the electrochemical reaction.[6] Furthermore, sulfur is abundant, cost-effective, and environmentally benign, making Li-S batteries an attractive alternative for sustainable energy storage solutions. Despite these advantages, the commercialization of Li-S batteries faces several challenges. A major challenge in Li-S batteries is the "shuttle effect", in which soluble lithium polysulfides (Li_2S_x, $4 \le x \le 8$) diffuse between the cathode and anode during cycling, resulting in active material loss, reduced Coulombic efficiency, and rapid capacity fading.[7] Additionally, the insulating nature of sulfur and its discharge products (Li_2S_2/Li_2S) results in poor electrochemical utilization and sluggish reaction kinetics. The conversion of S_8 to Li_2S induces significant volumetric expansion, causing mechanical degradation of the cathode structure and loss of electrical contact, exacerbating the stability and safety concerns of Li-S batteries.[8]

To address these challenges, extensive research has been devoted to optimizing the cathode architecture, designing advanced electrolytes, and developing protective strategies for the lithium anode.[9–12] Innovations such as sulfur-carbon composites, conductive polymer coatings, and nanostructured host materials have shown promise in enhancing sulfur

[a] Rubber Technology Centre, Indian Institute of Technology Kharagpur, India - 721302.
[b] Department of Physics, School of Basic Sciences, Indian Institute of Technology Bhubaneswar, India – 752050
[c] School of Nano Science and Technology, Indian Institute of Technology Kharagpur, India - 721302

View Article Online
DOI: 10.1039/D5CY00275H

utilization and mitigating the shuttle effect.[13,14] Similarly, the introduction of porous cathode host materials, solid-state electrolytes, additives, and artificial solid-electrolyte interphases (SEIs) has improved the safety and cycling stability of Li-S batteries.[15–20] Despite these advancements, achieving a balance between high energy density, long cycle life, and cost-effectiveness remains a critical hurdle.

Recently, alternative sources of sulfur have been used to minimize the leaching of sulfur from the cathode during operation. Once sulfur is bound to an organic moiety, for instance, a polymer, the leaching of sulfur during charge-discharge could be restricted. Thus, such approaches could open up possibilities such as sulfur bound covalently to carbon-based materials derived from polyacrylonitrile, giving sulfurized polyacrylonitrile (SPAN) with high specific capacities and high cycle stabilities.[21,22] The pioneering work of Pyun *et al.* introduced a revolutionary method that has transformed the utilization of elemental sulfur by enabling the synthesis of stable sulfur-rich polymers, which are referred to as "inverse vulcanization".[23,24] This method involves terminating the bi-radicals of sulfur at the ends of polysulfide chains by crosslinking them with diene-based crosslinkers.[25] Unlike conventional vulcanization, which typically incorporates small amounts of sulfur into organic polymers, inverse vulcanization uses sulfur as the primary component, yielding polymers with high sulfur content. The resulting sulfur-rich polymers exhibit enhanced thermal and chemical stability, making them particularly promising for multiple applications, including in Li-S batteries, heavy metal remediation, organic contaminant removal lenses of infrared thermal imaging cameras, self-healing and shape memory polymers, controlled release fertilizers, and antibacterial coatings applications.[26–32] Among these applications, inversely vulcanized polymers have emerged as highly promising candidates for the development of advanced cathode materials in Li-S batteries, demonstrating significant potential to extend battery life and enhance electrochemical performance.[33–37]

The redox transformation mechanism in inversely vulcanized polymers proceeds primarily through an organosulfur pathway, which resembles the electrochemical processes observed in conventional Li-S batteries. The stable carbon-sulfur (C-S) framework within these macromolecules is critical in enhancing the cathode material's structural integrity and electrochemical performance. A key advantage of inverse vulcanization lies in its ability to chemically confine sulfur within a robust polymeric matrix, effectively mitigating the polysulfide shuttle effect, a predominant cause of capacity degradation in traditional Li-S batteries. This confinement strategy minimizes the dissolution and migration of polysulfide intermediates, thereby improving cycling stability, sulfur utilization, and overall battery performance. Additionally, by crosslinking sulfur with organic molecules, the resulting sulfur-rich polymers exhibit improved mechanical integrity and reduced polysulfide solubility in the electrolyte.[38] The type of co-monomer and its feed ratio, and the sulfur rank (number of sulfur atoms between two carbon atoms) in the inversely vulcanized polymers have been found to significantly influence the performance of Li-S batteries.[39] Since the introduction of inversely vulcanized polymers as cathode materials for Li-S batteries, extensive research efforts have been directed toward this field to use various co-monomers to synthesize them, aiming to optimize their electrochemical properties and enhance battery performance.[27] By leveraging the unique properties of sulfur-rich polymers, inverse vulcanization offers a promising pathway to address the inherent challenges of Li-S batteries, enabling the development of more efficient and durable energy storage systems.

Conventional inverse vulcanization has been demonstrated to be effective for vinyl monomers with boiling points either above or near the reaction temperature of the inverse vulcanization and having non-polar characteristics. The challenge persists when exploring polar or low-boiling-point monomers in uncatalyzed inverse vulcanization. Often, phase separation occurs when a polar monomer is injected into the inverse vulcanization system, as the non-polar sulfur melt loaded with sulfur diradicals is less likely to attack the bulk comonomer, and thus only a little or no copolymer of sulfur and the polar monomer forms. Catalytic inverse vulcanization, introduced by Wu et al., has expanded the scope of sulfur copolymerization by facilitating the incorporation of polar monomers that are otherwise unreactive in conventional inverse vulcanization processes.[40] In one hand, the commonly used vulcanization accelerator serves as a compatibilizer or a phase transfer catalyst between sulfur melt and organic monomer and helps in producing copolymer with high amount of organically bound sulfur.[41] On the other hand, the inclusion of polar monomers introduces heteroatoms into the polymer backbone, which can increase Li-ion flux across the electrode and render more sulfur-rich copolymers electrochemically active. These heteroatoms in the backbone improve the affinity of the cathode material for lithium ions, facilitate ion transport, and provide additional binding sites to mitigate the polysulfide shuttle effect.[42,43]

In this work, an inversely vulcanized polymer containing flexible oligo-ethylene units was synthesized following catalytic inverse vulcanization route between triethyleneglycol dimethacrylate and sulfur. To facilitate the formation of a high fraction of organically bound sulfur, zinc diethyldithiocarbamate was opted to serve as a catalyst in this study from a long list of available vulcanization accelerators due to its recognition as an ultrafast accelerator in rubber vulcanization.[41] The successful formation of the copolymer through catalytic inverse vulcanization is confirmed using FT-IR, Raman, XPS, XRD, TGA, and DSC analyses. Understanding the mechanistic insights into inverse vulcanization was not explored in-depth through theoretical prediction. The feasibility of inverse vulcanization via a catalytic pathway was assessed through theoretical studies, including structural optimization, stability, and potential for bond formation. Based on the minimum or no unreacted sulfur to organic co-monomers, the best copolymer was hybridized with MWCNTs, considering the insulating nature of the prepared copolymers. A reference sample of pristine sulfur was also prepared while keeping the sulfur and MWCNT ratio the same. The

View Article Online
DOI: 10.1039/D6CY00375H

morphological studies of the copolymer electrodes were conducted using SEM and TEM analysis. EDAX and CHNS(O) analysis were performed in order to ascertain the homogeneous distribution of sulfur-rich copolymer and MWCNT. The copolymer was used as an active cathode material to prepare 2032-type Li-S coin cells. TEGDMA-based cells demonstrated substantially improved capacity retention after 100 charge/discharge cycles and superior rate capability relative to conventional sulfur-based cathodes.

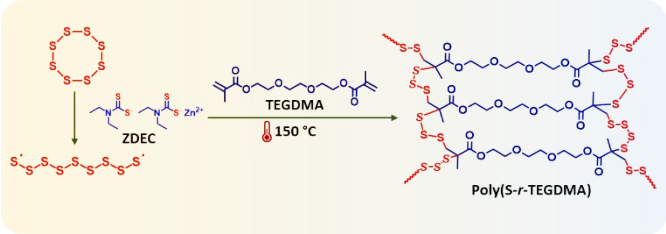

Fig. 1. Scheme for the synthesis of Poly(S-*r*-TEGDMA) via catalytic inverse vulcanization using Zinc diethyldithiocarbamate.

2. Experimental Section

2.1. Materials

Sulfur powder (99%, Ramkem, India) was used as received. The monomer triethyleneglycol dimethacrylate (TEGDMA, 98%) was procured from Sigma Aldrich, USA, and purified before use by passing through a column filled with basic Alumina. Zinc diethyldithiocarbamate (ZDEC) was procured from IOCL, India, and recrystallized in chloroform before use. *N*-methyl-2-pyrrolidone (NMP) was procured from TCI chemicals. MWCNTs (NC7000™) were obtained from Nanocyl SA, Belgium. The battery grade electrolytes lithium bis(trifluoromethane-sulfonyl)imide (LiTFSI, 99.99%) and lithium nitrate ($LiNO_3$, 99.99%), the binder polyvinylidene fluoride (PVDF, M_w~530,000 g·mol^{-1}), and battery grade solvents 1,3-dioxolane (DOL) and 1,2-dimethoxyethane (DME) were purchased from Sigma Aldrich and used as received. CR-2032 coin cell parts, and lithium disc of diameter 15 mm were procured from Sinsil International Private Limited and stored in argon filled glove box (Ranvac Technologies Private Limited).

2.2. Characterization

The functional groups and structural properties of the synthesized copolymers were characterized using Fourier Transform Infrared Spectroscopy (FT-IR, PerkinElmer, Model Spectrum 2, Singapore) in Attenuated Total Reflection (ATR) mode, within a spectral range of 4000–400 cm^{-1}. The resolution was maintained for each sample at 4 cm^{-1} and 8 scans were performed for each sample. Raman spectra were captured by employing a Raman spectrometer (Jobin Yvon Horiba, France), utilizing an Ar:Kr mixed ion gas laser with an excitation wavelength of 532 nm. To achieve a spectral resolution of approximately 1.2 cm^{-1}, a grating with 1800 grooves per mm and a 20x objective was employed. The laser spot on the sample had a diameter of about 1 mm at a power of 0.2 mW at the focal point. Each spectrum was acquired with an acquisition time of 10 s, and 20 accumulations were taken. The elemental chemical states of the copolymers were determined using X-ray Photoelectron Spectroscopy (XPS, PHI 5000 VERSA PROBE III, ULVAC PHI, USA). The surface morphology and porosity were examined through Field Emission Scanning Electron Microscopy (FE-SEM, ZEISS Sigma 300 VP, Germany). Before analysis, the samples were fragmented into small pieces and vacuum-dried for 24 h. For FE-SEM imaging, the samples were coated with an Au-Pt alloy (approximately 1–3 nm thick) using a sputter coater (Quorum, Q150R S). Elemental composition analysis of the samples was conducted using Energy Dispersive X-ray (EDAX) spectroscopy and FlashSmart™ CHNS(O) Elemental Analyzer (Thermo Fisher Scientific Inc). Transmission electron microscopy (TEM) was performed using a Libra 200 system (Carl Zeiss GmbH, Oberkochen, Germany) operated at an accelerating voltage of 200 kV. For sample preparation, a small quantity of the hybrid powder was ultrasonically dispersed in ethanol. A drop of the resulting suspension was deposited onto a lacey carbon-coated copper grid and subsequently dried on a hot plate prior to imaging. The phase composition of the samples was analyzed using X-ray diffraction analysis (XRD, Bruker D2 Phaser 3). The thermal properties of the samples were evaluated using a Differential Scanning Calorimeter (DSC, TA Instruments DSC25). Approximately 8 ± 2 mg of each sample was sealed in Tzero aluminium hermetic pans and analyzed under a nitrogen flow of 350 ± 10 mL·min^{-1}. The heating and cooling rate was set to 10 °C·min^{-1}, and thermal transitions were recorded over a temperature range of -80 °C to 180 °C. The glass transition temperature (T_g) was determined as the midpoint of the endothermic transition during the second heating cycle. The thermal stability and degradation behaviour of the synthesized copolymers were assessed using thermogravimetric analysis (TGA, Shimadzu TGA-50). About 10 mg of each sample was placed in a platinum pan and analyzed from 30 °C to 800 °C at a heating rate of 20 °C·min^{-1} under a nitrogen atmosphere.

2.3. Synthesis of Poly (Sulfur-*r*-Triethyleneglycol dimethacrylate)

A pre-weighed quantity of sulfur powder (700 mg, 2.73 mmol) was thoroughly blended with ZDEC (0.15 g, 0.414 mmol) using a mortar and pestle to obtain a homogeneous mixture. The resulting blend was transferred into a 40 mL glass vial equipped with a magnetic stirring bar and subsequently heated to 150 °C in an oil bath under continuous stirring at 500 rpm. Upon complete melting of the sulfur matrix, the predetermined amount of TEGDMA was promptly injected into the molten mixture. The stirring rate was then increased to 900 rpm to ensure uniform dispersion and facilitate the reaction. On the addition of TEGDMA, a slight decrease in the temperature of 1 to 2 °C was observed on the thermocouple. Nevertheless, the reaction temperature promptly returned to the set value within 2-3 min and remained stable till the end of the reaction. Initially, a phase separation was observed between the TEGDMA and molten sulfur. This type of phase

separation remains always in the absence of ZDEC as mediator. (**Fig. S1A, Supporting Information**). However, the mixture eventually turned into a homogeneous solution. The completion of the reaction was noted as soon as the magnetic stirring stopped automatically. Vitrification time is recorded as the point at which monomer addition to the formation of solid products. The polymer was extracted, powdered and washed with ethanol to remove any unreacted monomer and residual ZDEC from the copolymeric system and dried under vacuum at 70 °C for 12 h. Three copolymers were prepared by maintaining a constant molar ratio of sulfur to TEGDMA, while systematically varying the ZDEC concentration at 1 wt.%, 3 wt.%, and 5 wt.% by weight. The copolymers were designated using the nomenclature $S_xDMA_yZ_z$, where x and y denote the weight percentages of sulfur (fixed at 70 wt.%) and TEGDMA (30 wt.%), respectively. The subscript z corresponds to the weight percentage of the ZDEC, varied systematically at 1 wt.%, 3 wt.%, and 5 wt.% relative to the combined weight of sulfur and TEGDMA.

2.4. Computational analysis via Density Functional Theory (DFT)

Density functional theory (DFT) calculations were carried out using the Gaussian 16 software package. All molecular geometries were optimized at the M06-2X/6-311+G(d,p) level of theory employing an ultrafine integration grid, followed by vibrational frequency analysis to confirm the nature of the stationary points.[44] Closed-shell singlet calculations were used for ground-state structures, while spin-polarized calculations were employed to describe open-shell configurations associated with bond cleavage and radical formation. Transition-state structures were identified by a single imaginary frequency, and intrinsic reaction coordinate calculations were performed to confirm the connectivity between reactants and products. Gibbs free energies were obtained from the thermal corrections at the same level of theory.

2.5. Electrode fabrication, cell assembly and electrochemical characterizations

The electroactive copolymer and MWCNT were hand-milled at 80:20 ratio in a mortar to form a hybrid composite material. The $S_{70}DMA_{30}Z_5$/MWCNT composite mixture is then mixed with 5 wt.% PVDF binder in NMP to form a homogenous cathode slurry. The slurry was deposited uniformly onto a nickel foil substrate, initially dried in a fume hood, and subsequently transferred to an oven for extended drying at 60 °C overnight to eliminate any residual solvent. Circular cathodes with an area of ~1.5 cm^2 were precisely cut using crimping equipment. The areal sulfur loading was maintained within 5-7 $mg{\cdot}cm^{-2}$. The electrode and other components are assembled into CR-2032 coin cells. The assembly included a Whatman glass fibre separator, Celgard® 2325 trilayer separator, a lithium foil anode, copper current collector, spacer, and spring. The electrolyte is composed of 1 M LiTFSI and 0.25 M $LiNO_3$ in a 1:1 v/v mixture of DOL and DME. The electrolyte-to-sulfur ratio was maintained at 9-10 $mL{\cdot}g^{-1}$ during cell assembly. The components were carefully integrated inside an Argon-filled glovebox (O_2 < 0.1 ppm, H_2O < 0.1 ppm) to ensure proper cell configuration and functionality. The reference electrodes based on sulfur and MWCNT were also fabricated using an identical processing protocol while maintaining comparable thickness and sulfur loading. These high-loading, thick electrodes are critical for achieving the areal capacities necessary to meet the energy density requirements of electric vehicle applications. Electrochemical benchmarking of the prepared cells was conducted over a voltage window of 1.8 V to 2.6 V versus Li^+/Li. The electrical conductivity of the active material composite was measured using the Ossila four-point probe conductivity meter. For the conductivity measurement, the cathode slurry was coated on a Kapton film (11 mm diameter) with a coating thickness of *ca.* 80 µm. Cyclic voltammetry (CV) was performed at a scan rate of 0.1 $mV{\cdot}s^{-1}$. Electrochemical impedance spectroscopy (EIS) was conducted in the frequency range of 1 MHz to 10 mHz with an applied voltage amplitude of 5 mV. Both CV and EIS experiments were undertaken in the Pine WaveDriver 200 electrochemical workstation. Galvanostatic charge-discharge (GCD) measurements were carried out using Neware 8-channel battery tester at a current rate of 0.1C. The rate handling performance of the cells was studied at various specific currents, corresponding to charge/discharge rates ranging from 0.2, 0.5, 1, 2C, and returned to 0.2C, where 1C is equivalent to 1675 $mAh{\cdot}g^{-1}$. GITT analysis was performed to evaluate the Li^+ diffusion kinetics of the fabricated CR2032 coin cells. A constant-current pulse at a low current density was applied to the cell for 15 min. This was followed by an open-circuit relaxation period of 30 min to allow the cell voltage to reach a quasi-equilibrium state. This pulse–relaxation sequence was repeated stepwise over the voltage range (1.8–2.35 V) during both discharge and charge processes.

3. Results and discussion

Catalytic inverse vulcanization allows the synthesis of sulfur-based copolymers having heteroatoms bearing polar monomers, which are unreactive to sulfur. In this study, copolymers of sulfur and TEGDMA were successfully synthesized using ZDEC at a temperature of 150 °C which is below the floor temperature (159 °C) of sulfur. ZDEC belongs to the class of dithiocarbamates, which are widely used as accelerators in the rubber vulcanization processes. Metal-free molecules exhibit poor or non-catalytic activity, suggesting that the metal cation is crucial.[41]

It is believed to be important for binding either sulfur or the comonomer. Coordination to the metal centre may weaken S-S bonds, explaining why catalytic inverse vulcanization occurs at lower temperatures than uncatalyzed reactions, which typically require high temperatures for homolytic cleavage of the S-S bond. The DEDC (diethyldithiocarbamate) ligand itself may assist in the cleavage of S-S bonds and C=C bonds by acting as a nucleophile. This nucleophilic behaviour further contributes to

View Article Online
DOI: 10.1039/D5CY00375H

the lower reaction temperatures observed in catalytic inverse vulcanization. A plausible mechanism for the catalytic inverse vulcanization of sulfur with TEGDMA, facilitated by ZDEC, has been proposed based on the work of Dodd et al. and is illustrated in **Fig. S2 (supporting information)**.

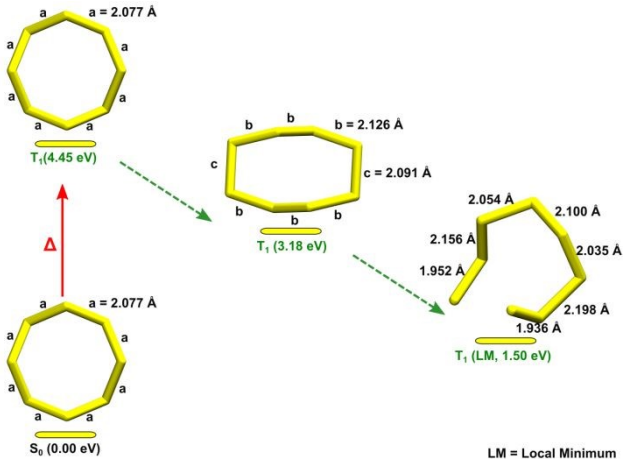

Fig. 2: Structural evolution of the S_8 ring from the closed-shell singlet configuration (S_0) to open-shell (triplet-like) configurations obtained using (unrestricted) DFT at the M06-2X/6-311+G(d,p) level of theory

The equilibrium structure of the S_8 ring was first optimized at the chosen level of DFT and adopts a symmetric crown-shaped cyclic geometry with uniform S-S bond lengths of 2.077 Å. The singlet state corresponds to the most stable configuration at the equilibrium geometry of the S_8 ring. [45–48] To investigate the S-S bond dissociation process and the associated changes in electronic structure, a potential energy surface scan was performed along the selected S-S bond coordinate. The singlet potential energy surface exhibits a monotonic increase in energy upon bond elongation (**Fig. S3**, supporting information), indicating that bond dissociation is not adequately described within a closed-shell framework. Since homolytic S-S bond cleavage leads to the formation of radical species.[40,41] spin-polarized calculations were employed as a computational model to describe the associated open-shell configurations. [49–51] These calculations show noticeable S-S bond elongation and partial ring opening, accompanied by charge redistribution among sulfur atoms (**Fig. 2**), consistent with the development of radical character during sulfur activation. The energy difference between the closed-shell singlet and the open-shell configurations is approximately 1.50 eV (144.7 kJ·mol^{-1}), reflecting the energetic cost of reactive open-shell states.

Furthermore, the interaction between ZDEC and sulfur was examined to understand its role in sulfur activation. The optimized ground-state S_8-ZDEC complex remains structurally stable without spontaneous S-S bond cleavage. However, upon adopting an open-shell configuration, the system undergoes structural rearrangement with partial S-S bond elongation. This behavior indicates that sulfur activation is associated with the development of radical character rather than direct ground-state coordination. [52] The calculated energy difference (~1.39 eV, 134.11 kJ·mol^{-1}) indicates the energetic separation between the closed-shell and open-shell configurations associated with sulfur activation (**Fig. 3**).

The reduced energy gap in the presence of ZDEC suggests that sulfur can more readily access reactive open-shell configurations. These results provide qualitative evidence for the role of ZDEC in promoting sulfur activation and influencing its reactivity toward subsequent reactions with the monomer.

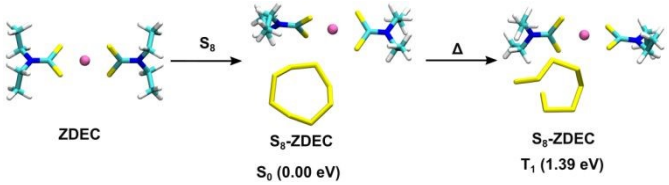

Fig. 3. Optimized structures of the S_8-ZDEC system in closed-shell and open-shell configurations

To model the initiation step of inverse vulcanization, the interaction between sulfur species and the TEGDMA monomer was investigated. The Gibbs free energies (G) of the reactant, transition state, and product along the reaction pathway were calculated. Frequency analyses were performed following geometry optimizations at the same level of theory to confirm the nature of the stationary points; minima corresponding to the reactant and product exhibit no imaginary frequencies, whereas the transition state is characterized by a single imaginary frequency.

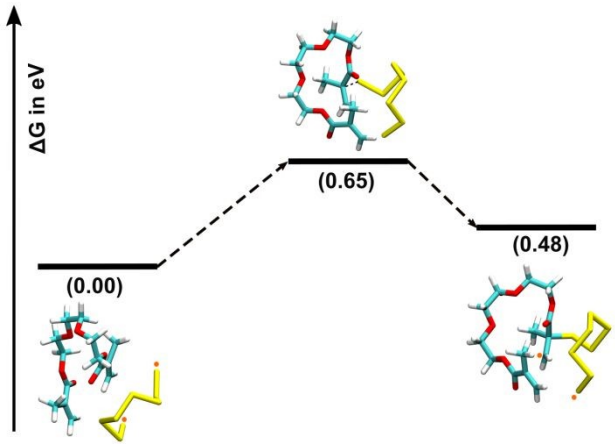

Fig. 4 Reaction free energy profile for the interaction between TEGDMA and activated sulfur species derived from S_8.

The transition state (TS) obtained for the S_8-TEGDMA system represents the interaction of activated sulfur with the C=C bond of the monomer (**Fig. 4**). The reaction proceeds via a partial C-S bond, as indicated by a single imaginary frequency and a C-S bond distance of 2.267 Å. As shown in **Fig. 4**, the calculated free energy profile indicates an activation barrier of 0.65 eV (62.7 kJ·mol^{-1}), suggesting that the reaction is kinetically accessible. The optimized product exhibits a C-S bond length of approximately 1.851 Å. NBO analysis further confirms the formation of the C-S bond, as evidenced by the presence of a σ(C-S) bonding orbital with an occupancy of 0.98, indicating the development of a bonding interaction

View Article Online
DOI: 10.1039/D5CY00275H

between sulfur and the monomer. Such C-S bond formation is consistent with radical-mediated addition of sulfur species to monomers. [53] The resulting structure retains radical character, with an unpaired electron density distributed between the terminal sulfur atom and the adjacent carbon center, indicating the possibility of further propagation reactions (**Fig. S4**, supporting information).

The free energy profile shows that the product of the initial C-S bond formation step is slightly higher in free energy than the separated reactants (ΔG = 0.48 eV or 46.3 kJ·mol^{-1}), reflecting entropic contributions associated with complex formation. However, the low activation barrier (ΔGa‡ = 0.65 eV) indicates that the reaction remains kinetically accessible under polymerization conditions. These results collectively suggest that sulfur activation leads to reactive species capable of initiating polymerization through radical-mediated C-S bond formation.

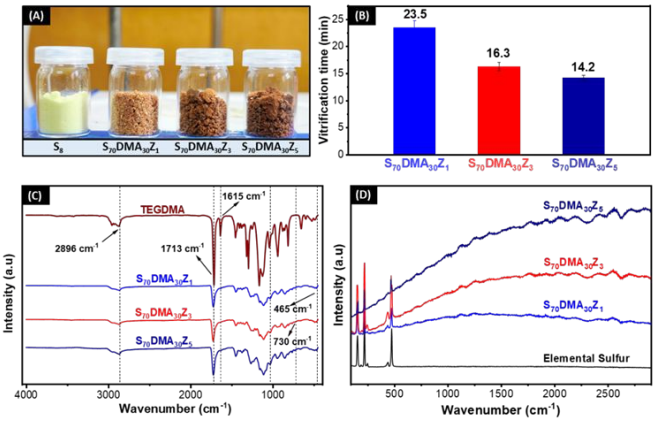

Fig. 5. (A) Digital photographs of the solid copolymers and elemental sulfur, (B) Vitrification time (C) FT-IR spectra of $S_{70}DMA_{30}Z_1$, $S_{70}DMA_{30}Z_3$ and $S_{70}DMA_{30}Z_5$ in comparison with TEGDMA, (D) Raman spectra of copolymers in comparison with elemental sulfur.

The copolymers were synthesized while keeping the sulfur to TEGDMA ratio at 70:30 in all the compositions with varying ZDEC feed ratios **(Fig. 5A)**. Several studies have demonstrated that inversely vulcanized polymers with a sulfur content between 60-70 wt.% exhibit low sulfur rank, which is optimal for achieving good electrochemical performance in Li-S battery applications.[54] This intermediate ratio minimizes unreacted sulfur residues, a common issue at higher sulfur concentrations, while maintaining sufficient active material content in the cathode, which is critical for achieving high capacity. No observable reaction occurred between TEGDMA and elemental sulfur under conventional inverse vulcanization (185 °C) conditions. Molten sulfur and TEGDMA remained phase-separated throughout the reaction, and no consumption of double bond was evident in the FT-IR analysis (**Fig. S1A-B,** Supporting Information).

Metal DEDCs are recognized to act as phase transfer agents between the immiscible sulfur and organic phases. The sulfur-containing dithiocarbamate group may have an affinity for the sulfur phase, while the alkyl chains interact with the organic phase. This allows the ZDEC to draw bound sulfur chains from the molten sulfur into the comonomer phase, where the reaction proceeds more readily. The presence of ZDEC can significantly shorten the biphasic stage of the reaction. The addition of just 1 wt.% ZDEC in the polymerization system enabled efficient polymerization, producing solid polymeric materials below the sulfur floor temperature.[55] The reaction reached completion within 23.5 min after monomer addition. Although solid copolymer formation was evident, residual unreacted sulfur was detected in the copolymeric system, as confirmed by DSC and XRD analyses, discussed in detail below. Increasing the ZDEC loading to 3 and 5 wt.% significantly accelerated the reaction kinetics, reducing the vitrification time to 19 and 14 min, respectively **(Fig. 5B).**

FT-IR analysis was used to identify the functional groups present in the copolymer. The FT-IR spectra of the monomer TEGDMA, three copolymer systems, each synthesized with varying contents of the ZDEC, are presented in **Fig. 5C**. A prominent absorption peak at 1615 cm^{-1}, corresponding to the vinylidene functional group, was observed in the monomer spectrum. Notably, this peak is absent in the FT-IR spectra of all three copolymer systems, providing clear evidence of the involvement of the double bonds in the inverse vulcanization reaction. In addition, the emergence of a characteristic peak at 730 cm^{-1} (weak intensity) and 465 cm^{-1} attributed to the C-S and S-S stretching vibrations further corroborates the successful inverse vulcanization process between sulfur and TEGDMA.[56] The addition of sulfur to the TEGDMA moiety was further confirmed using Raman spectroscopy. Raman spectra of the copolymers in comparison to elemental sulfur are provided in **Fig. 5D**. Elemental sulfur shows sharp peaks at 151 cm^{-1} and 215 cm^{-1} due to the S–S bending and at 471 cm^{-1} due to the S–S stretching vibrations. In addition, the broad bands in the range of 600-800 cm^{-1} are indicative of C-S stretching vibration in the copolymer.[57,58] These vibrational peaks confirm the formation of polysulfide bonds, highlighting the successful integration of sulfur into the copolymer framework.

XPS analysis was also conducted to confirm the successful inverse vulcanization between sulfur and TEGDMA. The XPS survey scan of $S_{70}DMA_{30}Z_5$, along with the corresponding high-resolution spectra, is presented in **Fig. 6**. The elemental survey scan of $S_{70}DMA_{30}Z_5$ exhibits four distinct peaks at binding energies of 284 eV, 531 eV, 226 eV, and 163 eV, corresponding to C 1s, O 1s, S 2s, and S 2p, respectively **(Fig. 6A)**. The deconvolution of the C 1s, S 2p, and O 1s peaks into their respective chemical components was carried out using Gaussian fitting. The C 1s region of the copolymers was deconvoluted into four distinct peaks, with binding energies assigned as follows: 284.4 eV corresponding to the sp^2 hybridized C-C bond, 285.61 eV attributed to carbon in the C-O-C bond (associated with ester functionality), and 288.3 eV attributed to the carbonyl carbon (C=O) in the TEGDMA chain.[34] Furthermore, a peak at 286.1 eV, corresponding to the binding energy of the C-S bond, indicates the successful inverse vulcanization between sulfur and TEGDMA **(Fig. 6B)**. Moreover, the S 2p spectrum of $S_{70}DMA_{30}Z_5$ displays two distinct peaks at 162.8 eV and 164 eV, corresponding to

binding energies of -S-S- and C-S bonds, respectively **(Fig. 6C)**. Additionally, the peaks observed at binding energies of 531.4 eV and 532.4 eV in the O 1s high-resolution spectra of $S_{70}DMA_{30}Z_5$ further confirm the presence of C-O-C and C=O bonds in the TEGDMA moiety **(Fig. 6D)**. These findings provide further evidence for the successful integration of sulfur species into TEGDMA through inverse vulcanization.

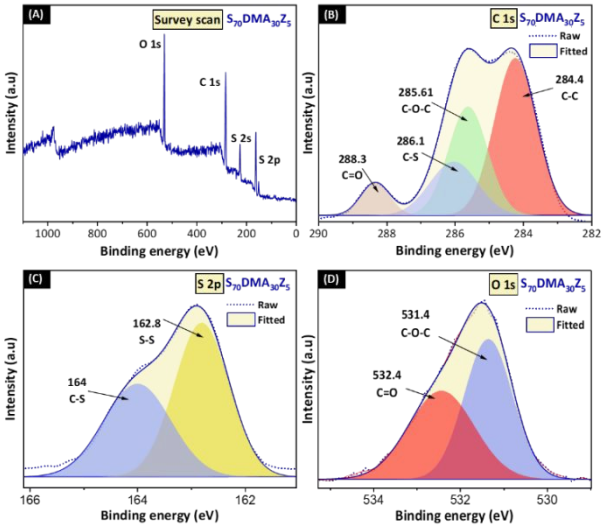

Fig. 6. X-ray photoelectron spectra of $S_{70}DMA_{30}Z_5$ (A) survey scan, (B) C 1s high resolution spectra, (C) S 2p high resolution spectra, and (D) O 1s high resolution spectra.

XRD analysis was employed to evaluate the scattering patterns of the synthesized copolymers. The X-ray diffractograms of copolymers in comparison with elemental sulfur is plotted in **Fig. 7A**.

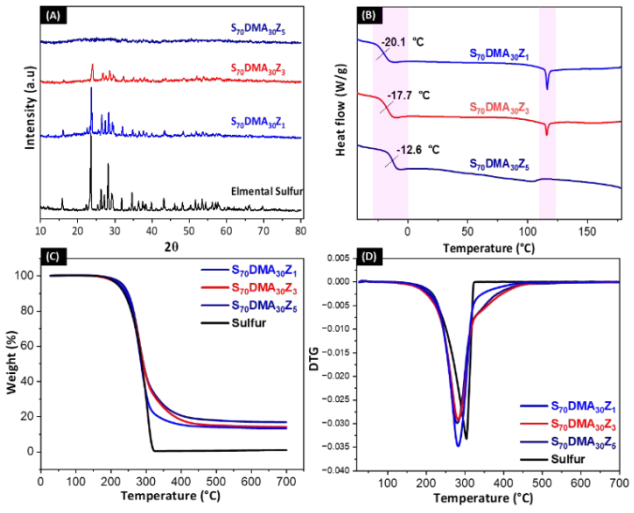

Fig. 7. (A) X-ray diffractograms of the three copolymers and elemental sulfur, (B) DSC, (C) TGA, and (D) DTG thermogram of the synthesized copolymers and elemental sulfur.

The X-ray diffractogram of elemental sulfur displays prominent and well-defined peaks at 2θ values of 23°, 28°, 29°, 52°, and 54°, indicative of a highly ordered crystalline structure.[59] The copolymers, $S_{70}DMA_{30}Z_1$ and $S_{70}DMA_{30}Z_3$, also showed the characteristic diffraction patterns of elemental sulfur with slightly reduced intensity, pointing to the presence of some unreacted sulfur within the copolymeric system. In the case of the copolymer synthesized using 5% ZDEC, the copolymer showed no diffraction pattern similar to sulfur, which implies that all the feed sulfur took part in the reaction, yielding a highly crosslinked amorphous copolymer. The ZDEC exhibited distinct, sharp crystalline peaks in its pristine form at 10.10, 12.12, 14.42, 17.62, 20.19, 20.86, 23.56, 24.38, 31.64, and 33.42° **(Fig. S5, supporting information).**[60] Notably, these characteristic peaks are also completely absent in all copolymeric systems, indicating that ZDEC was fully consumed during the inverse vulcanization process. The absence of residual crystalline ZDEC in the final products confirms its effective participation in the reaction.

DSC is used to obtain insights into the thermal response of the polymer over the temperature range of -50 °C to 150 °C, as shown in **Fig. 7B**. Elemental sulfur exhibits two distinct crystalline melting endotherms. The first endotherm, observed at approximately 109 °C, corresponds to the melting of α-S_8, which involves a phase transition from the orthorhombic to the monoclinic structure. This is followed by a second endotherm at approximately 120 °C, attributed to the melting of β-S_8 **(Fig. S6, Supporting Information).**[41] In the case of the copolymers, the appearance of a glass transition temperature confirms the formation of a polymeric material through catalytic inverse vulcanization reaction between sulfur and TEGDMA. The copolymer $S_{70}DMA_{30}Z_1$, showed a glass transition temperature (T_g) at -19.5 °C. Along with the appearance of T_g, the copolymer exhibited a melting peak (T_m) at 117 °C, which is consistent with the melting behaviour observed in elemental sulfur, indicating the presence of some amount of unreacted sulfur within the copolymeric system. For the copolymer $S_{70}DMA_{30}Z_3$, the T_g was observed to shift to a higher value of -17.5 °C, accompanied by a less intense melting endotherm at 117 °C compared to that of $S_{70}DMA_{30}Z_1$. It is plausible that the addition of a higher ZDEC loading likely enhances crosslinking efficiency, promoting a more uniform sulfur distribution within the polymer network. This results in shorter polysulfide linkages between crosslink points, thereby increasing the T_g of the material.[40] Additionally, an increased amount of ZDEC facilitates the incorporation of a greater proportion of the monomer into the inverse vulcanization reaction. The copolymer $S_{70}DMA_{30}Z_5$, synthesized with 5 wt.% ZDEC demonstrated a T_g at -12.6 °C and showed no trace of crystalline melting endotherm, indicating that all the feed sulfur was fully transformed into an amorphous state and effectively integrated into the monomer via inverse vulcanization. Additionally, the observed increase in T_g may be attributed to the preferential formation of short-chain polysulfide linkages between the carbon atoms of the monomer, rather than extended polysulfide chains. This structural configuration promotes a higher crosslink density within the copolymer network, thereby enhancing its T_g.

TGA was conducted to evaluate the thermal stability of the synthesized copolymers. TGA and DTG (rate of change of mass with respect to temperature) thermogram of the copolymers in comparison to that of elemental sulfur is shown in **Fig. 7C-D.**

The onset of degradation is denoted as T_{95}, which represents the temperature at which 5 wt.% weight loss occurs. Elemental sulfur showed a single-step degradation with T_{95} at 220 °C, with a sharp drop in mass, and full weight loss occurred at a temperature of 320 °C, leaving no residue at the end of the TGA cycle. The copolymers also exhibited a single-step degradation process. However, unlike the sharp mass loss observed in elemental sulfur, they display broad decomposition profiles, with the maximum weight loss occurring at approximately 450 °C. The broad decomposition temperature observed in the copolymers is likely attributed to the degradation of sulfur-carbon (C-S) bonds and the cleavage of sulfur-sulfur (S-S) bonds. All copolymers exhibit residual char content at the end of the TGA cycle, which correlates with the carbon content of the comonomer. An increased amount of char content is observed for $S_{70}DMA_{30}Z_5$ (17 wt.%) compared to $S_{70}DMA_{30}Z_1$ (13 wt.%), suggesting that a substantial incorporation of comonomer occurred during the inverse vulcanization process when the ZDEC concentration was elevated from 1 wt.% to 5 wt.%. This indicates that the higher ZDEC content facilitated the comonomer's more effective participation in the reaction. Besides, TGA under inert atmosphere also provides indication of approximate sulfur content within the composite materials as the mass loss is majorly attributed to the decomposition of sulfur and organic residues left before char formation. For $S_{70}DMA_{30}Z_5$, the mass loss of 83 % can be correlated to the sum of mass loss occurred due to the volatile organic fraction and sulfur from which actual sulfur content is difficult to obtain. The knowledge of actual sulfur content in the composite is essential to set the current densities during constant current charge-discharge experiments. Although the absence of crystalline elemental sulfur in the polymer was confirmed by XRD and DSC analyses, these techniques are not sufficient to detect the presence of amorphous sulfur (dark sulfur) within the copolymer matrix. [61] Therefore, the bound sulfur content was quantified using Soxhlet extraction in toluene (see Supporting Information). The extraction resulted in only a negligible weight loss, indicating that sulfur in the copolymer predominantly exists in the bound form. In order to ascertain the actual sulfur content as well as the elemental composition in the composite, CHNS(O) analysis was carried out. The outcome of the results is presented in **Table S1**. The theoretical estimation was made considering the carbon, hydrogen, nitrogen, oxygen and sulfur contents in the reactants as copolymerization feed and in ZDEC. For reference sample, the theoretical calculation was done based on carbon and sulfur content in MWCNT and sulfur, respectively. The results show close matching of all the major elements in the reaction feed.

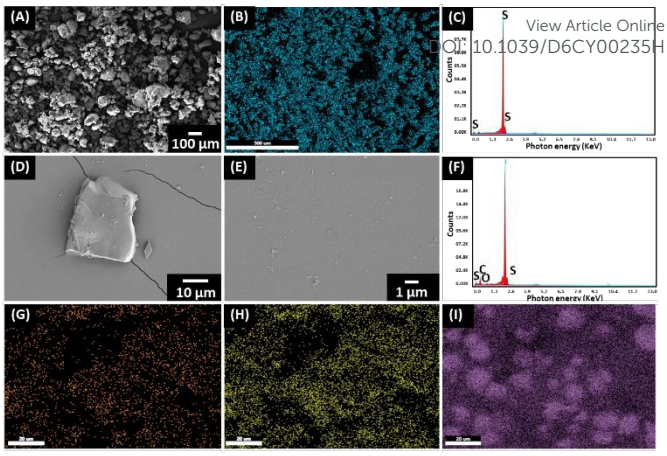

Fig. 8. (A) SEM image showing pristine of S_8 morphology, (B) corresponding E-DAX sulfur mapping, (C) EDAX sum spectrum of S_8, (D) and (E) surface morphology of $S_{70}DMA_{30}Z_5$, (F) corresponding EDAM sum spectrum, (G) Carbon, (H) Oxygen, and (I) Sulfur mapping of $S_{70}DMA_{30}Z_5$.

The morphological analysis of the surface and cross-section was examined using scanning electron microscopy coupled with energy dispersive x-ray analysis and shown in **Fig. 8.** Elemental sulfur showed heterogeneous morphology formed by the aggregation of small sulfur crystals (**Fig. 8A**). The EDAX sum spectrum of the crystalline sulfur sample reveals a highly intense peak at 2.307 keV, corresponding to the S-K_α emission line **(Fig. 8B-C)**. During the inverse vulcanization process, crystalline sulfur transforms into an amorphous state and becomes integrated into the monomer through the formation of C-S bonds. The SEM image of the $S_{70}DMA_{30}Z_1$ copolymer exhibits a smooth and homogeneous surface morphology **(Fig. 8D-E)**. EDAX with elemental mapping further confirms the elemental composition of the surface, revealing a sulfur-rich copolymer with a uniform distribution of carbon and oxygen (**Fig. 8F-I**).

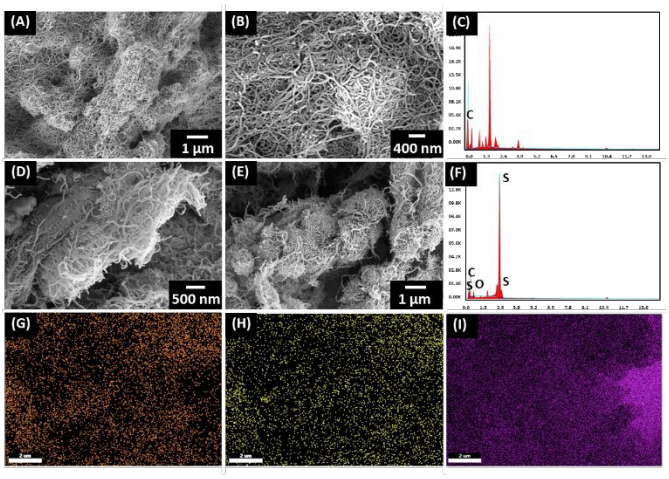

Fig. 9. (A) and (B) SEM images of MWCNTs at different magnifications and corresponding (C) EDAX sum spectrum of MWCNT, (D) and (E) SEM images of $S_{70}DMA_{30}Z_5$/MWCNT composite hybrids at different magnifications, (F) EDAX sum spectrum $S_{70}DMA_{30}Z_5$/MWCNT hybrids, (G), (H) and (I) represents the Carbon, Oxygen, and Sulfur elemental maps, respectively.

The porous structure of the cathode material plays an important role in the cyclic stability of a Li-S battery. The micropores can physically confine the insoluble lithium polysulfide species formed during the multiple redox reactions.[62] In this study, MWCNTs were used as the conducting host material for fabricating the cathode due to their high specific surface area (*ca.* 230 $m^2 \cdot g^{-1}$, pore volume 0.5 $cm^3 \cdot g^{-1}$) and pore size distribution covering majorly mesoporous regime with a little contribution from micropores **(Fig. S7, supporting information)**. The inter-tubular spaces around MWCNTs were utilized to be filled by the sulfur-rich copolymer in order to compensate for the low electrical conductivity of $S_{70}DMA_{30}Z_5$ and thus render the copolymer to participate in the redox processes in Li-S batteries. Besides, the tubular morphologies of MWCNTs could tightly hold the electrode mass with minimal binder addition. The SEM images of MWCNTs employed in this study exhibit a high aspect ratio, which facilitates effective intertwining between the polymeric active material and highly conducting MWCNTs within the composite matrix (**Fig. 9A-C**). The SEM image of $S_{70}DMA_{30}Z_5$/MWCNT composite demonstrates the homogeneous incorporation of MWCNTs within the copolymer matrix with minimal agglomeration, suggesting effective mixing (**Fig. 9D-F**). The MWCNTs are uniformly dispersed, forming a well-distributed network throughout the composite, which is critical for ensuring structural integrity and efficient electron transport in the electrode material. EDAX mapping further confirms the uniform distribution of sulfur within this hybrid matrix. **(Fig. 9G-I)**.

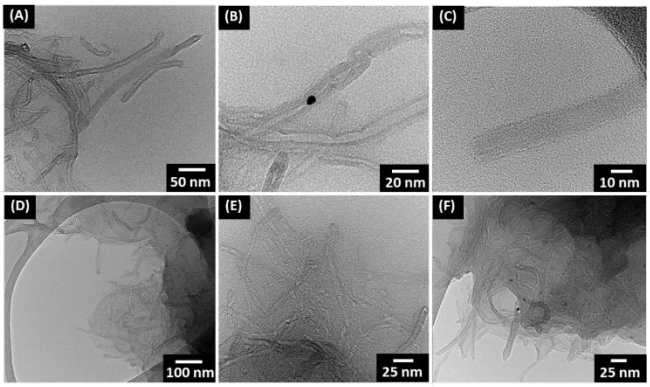

Fig. 10. High-resolution TEM images of (A-C) MWCNT, (D-E) $S_{70}DMA_{30}Z_5$/MWCNT hybrid composite

The comprehensive TEM analysis of the MWCNTs and the composite material is presented in **Fig. 10.** The TEM image reveals an interconnected network of nanotubes with an average diameter of around 10 nm, and sufficient inter-tubular spacing demonstrating excellent potential for creating a percolating conductive framework throughout the cathode structure (**Fig. 10A**). The hollow core structure, clearly visible in higher magnification images, provides essential nanoscale compartments for the active material infiltration and confinement, a critical feature for maintaining electrode integrity during cycling (**Fig. 10B-C)**. The TEM image of $S_{70}DMA_{30}Z_5$/MWCNT hybrid (**Fig. 10D-F)** reveals an intimate integration between the two components, where the MWCNTs form a three-dimensional interconnected conductive network throughout the active material matrix. Beyond their conducting role, the percolating MWCNT network functions as nanoscale reinforcing fibres, substantially enhancing the cathode's mechanical integrity.

Apart from the morphological studies, XRD also revealed the integration of MWCNTs into the amorphous polymer matrix. The XRD pattern of pristine MWCNTs exhibits a characteristic peak at ~25.7°, corresponding to the (002) reflection of graphitic carbon, along with a weaker peak at ~43° attributed to the (100) plane of hexagonal graphite. In contrast, the amorphous polymer alone shows a broad halo in the X-ray diffractogram, indicating its disordered structure. Upon blending the polymer with MWCNTs, the composite retains the broad amorphous signature of the polymer while displaying the distinct (002) reflection of MWCNTs, confirming their structural preservation within the matrix **(Fig. S8, Supporting information)**. However, the reduced intensity and slight broadening of the MWCNT peaks in the composite suggest partial exfoliation and uniform dispersion of the nanotubes within the polymer, which is critical for enhancing electrical conductivity and mechanical stability.

The electrochemical performance of the copolymer was investigated by using it as an active cathode material in CR-2032-type Li-S coin cells. The copolymer $S_{70}DMA_{30}Z_5$ is used for this purpose since it is the only composition that contains no crystalline sulfur, as revealed from XRD and DSC analysis in order to bypass any contribution from sulfur that remained unreacted with TEGDMA. The presence of crystalline sulfur may adversely affect the battery's electrochemical performance, as residual sulfur can promote detrimental polysulfide shuttling and rapid capacity fading. The conductivities of both $S_{70}DMA_{30}Z_5$/MWCNT and reference sample S_8/MWCNT were measured using a four-point probe conductivity meter and is found to be 354 ± 8 $S \cdot m^{-1}$ and 380 ±6 $S \cdot m^{-1}$, respectively. In both composites, a fixed content of 20 wt.% MWCNTs were used, which primarily govern the formation of the conductive network. As a result, both the polymer/MWCNT and sulfur/MWCNT composites exhibit comparable electrical conductivities, with only a marginal difference between them. The slightly higher conductivity of $S_{70}DMA_{30}Z_5$/MWCNT likely results from the improved dispersion of MWCNTs in the S-TEGDMA copolymer, which contrasts with the restrictive, crystalline structure of elemental sulfur.

The cyclic voltammogram of both S_8/MWCNT and $S_{70}DMA_{30}Z_5$/MWCNT-based cells exhibits characteristic redox features consistent with the electrochemical reactions of a Li-S cell. The cyclic voltammogram of both sulfur and TEGDMA-based electrodes is presented in **Fig. 11A-B**. During the lithiation process (discharge or reduction), the CV of S_8/MWCNT exhibits two characteristic cathodic peaks at ~2.37 V and ~1.96 V, corresponding to the sequential reduction of S_8 to soluble lithium polysulfides (Li_2S_n, $4 \leq n \leq 8$) and their subsequent conversion to insoluble short-chain lithium polysulfides (Li_2S_2/Li_2S). These short-chain lithium polysulfides

exhibit limited solubility in the liquid electrolyte due to their strong ionic interactions with Li^+ ions.[63]

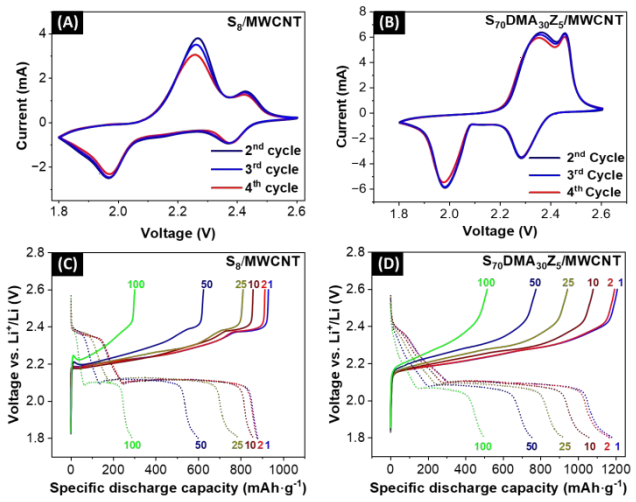

Fig. 11. (A) Cyclic voltammogram of (A) S_8/MWCNT cell and (B) $S_{70}DMA_{30}Z_5$/MWCNT-based cell. Galvanostatic charge–discharge curves recorded at 0.1C rate for (C) S_8/MWCNT and (D) $S_{70}DMA_{30}Z_5$/MWCNT-based cell.

During the anodic scan, two peaks at 2.26 V and 2.42 V arise from the reverse oxidation of long-chain lithium polysulfides back to short-chain polysulfides and eventually to S_8. During the cathodic sweep, $S_{70}DMA_{30}Z_5$/MWCNT exhibits two distinct reduction peaks at 2.28 and 1.98 V, corresponding to the stepwise reduction of organo-polysulfides to lithium-organo-polysulfide species. Conversely, the anodic sweep revealed oxidation peak at 2.36 V and 2.45 V, attributed to the reversion of lithium organo-polysulfides back to their parent organo-polysulfide. In comparison to the S_8/MWCNT electrode, the $S_{70}DMA_{30}Z_5$/MWCNT-based cells exhibit significantly improved electrochemical stability, as evidenced by the nearly overlapping CV curves over successive cycles. Moreover, the $S_{70}DMA_{30}Z_5$/MWCNT electrode delivers higher peak currents in CV relative to the S_8/MWCNT electrode. The increased current response indicates enhanced electrochemical activity, likely due to improved sulfur utilization and facilitated charge-transfer kinetics. Such characteristics are consistent with a more kinetically favourable redox process and improved electrochemical reversibility of the electrode.[64–66]

A critical concern regarding the use of organometallic compound in Li-S batteries is their potential involvement in redox side reactions or their instability within the operating voltage window. To evaluate the electrochemical innocence of the ZDEC, control electrodes were fabricated without the active sulfur copolymer (**Exp. S1**, supporting information). As shown in **Figure S9**, the CV profile of the MWCNT/ZDEC electrode exhibits no discernible redox peaks throughout the potential window applied for Li-S system. The current response remains essentially flat and featureless across the entire window, with current values hovering near zero (within ±0.01 mA), indicating the complete absence of any faradaic processes. The negligible capacitive current envelope observed is consistent with the minor electrochemical double-layer contribution from the MWCNT conductive framework, which is expected and inherent to carbon-based electrode materials.

Notably, no oxidation or reduction peaks attributable to ZDEC or its decomposition products are observed within the potential width of 1.8–2.6 V vs. Li^+/Li. This unambiguously confirms that ZDEC does not undergo any redox reactions, electrochemical activation, or side reactions under the conditions employed in Li–S battery operation if present even in traceable quantities. The electrochemical inertness of ZDEC within this voltage window establishes that the catalytic activity observed in the inverse vulcanization-derived sulfur copolymer cathode is purely of a chemical nature during polymer synthesis, and that ZDEC's presence in the final cathode material does not interfere with or contribute to the electrochemical charge–discharge processes of the Li–S cell.

The Galvanostatic charge-discharge voltage measurements of the prepared cells were conducted at a current density of 0.1C. The voltage profiles are displayed in **Fig. 11C-D**. The measurements reveal two well-defined voltage plateaus, corresponding to reduction and oxidation processes. Both electrodes exhibit two well-defined discharge plateaus, indicative of sequential reduction steps during the electrochemical process. Notably, the plateau potentials align precisely with the peak potentials observed in cyclic voltammetry. The sulfur electrode exhibits a theoretical specific capacity of 1,675 $mAh{\cdot}g^{-1}$. From the GCD curves, the discharge capacities of $S_{70}DMA_{30}Z_5$/MWCNT cathode are found to be 1182.2 $mAh{\cdot}g^{-1}$, while that of the sulfur-based electrode is only 879.1 $mAh.g^{-1}$. The TEGDMA-based electrode demonstrates superior active material utilization, achieving 70.6% of the theoretical capacity, whereas conventional sulfur-based electrodes attain only 51%.

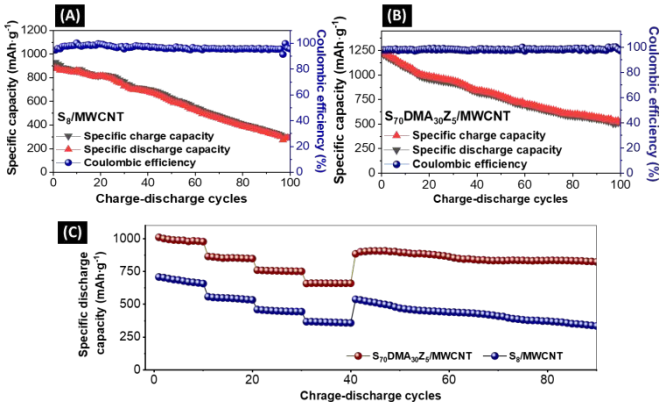

Fig. 12. Galvanostatic charge-discharge profile at 0.1C of (A) S_8/MWCNT, (B) $S_{70}DMA_{30}Z_5$/MWCNT, (C) rate capability studies of the S_8/MWCNT and $S_{70}DMA_{30}Z_5$/MWCNT. The specific capacities are normalized to the sulfur mass.

The GCD profile of the $S_{70}DMA_{30}Z_5$/MWCNT and S_8/MWCNT cathodes at 0.1 C (1C = 1675 $mAh{\cdot}g^{-1}$) is shown in **Fig. 12A-B.** The $S_{70}DMA_{30}Z_5$/MWCNT delivers an initial discharge capacity of 1182.2 $mAh.g^{-1}$ (Specific capacities are normalized to the sulfur mass) with a high coulombic efficiency of 97.8%. The cell retained a specific capacity of 501.7 $mAh.g^{-1}$

after 100 cycles, with a capacity decay of 0.53% per cycle and a coulombic efficiency of nearly 98%. On the other hand, the S_8/MWCNT cathode delivered an initial specific discharge capacity of 879.2 mAh.g^{-1} and retained only 287.3 mAh.g^{-1} after 100 cycles with a much faster capacity decay of 0.67% per cycle. The coulombic efficiency of the S_8/MWCNT cells at the 1st and last cycles were found to be 94.6 and 95.5%, respectively. Notably, the coulombic efficiency of the $S_{70}DMA_{30}Z_5$/MWCNT cells remained consistently high, never falling below 97% throughout the entire cycling study, which suggests high reversibility of the electrochemical reactions. This behaviour can be attributed to the robust integrated electrode architecture formed by the sulfur-TEGDMA copolymer and MWCNTs.

Rate capability and long-term cycling stability of the $S_{70}DMA_{30}Z_5$/MWCNT and S_8/MWCNT cathodes were systematically evaluated through a multi-step current density protocol (**Fig. 12C)**. Cells were initially cycled at 0.2C (10 cycles) to establish baseline performance, followed by stepwise increases to 0.5C, 1C, and 2C (10 cycles each) to assess high-rate behaviour, and finally, the current density was returned to a lower current rate of 0.2C (50 cycles). The $S_{70}DMA_{30}Z_5$/MWCNT composite cathode demonstrated excellent rate capability, delivering specific discharge capacities of 1009, 863.2, 758.5, and 656.8 mAh·g^{-1} at current rates of 0.2C, 0.5C, 1C, and 2C, respectively. Notably, when the current rate was restored to 0.2C, the cathode delivered a discharge capacity of 883 mAh·g^{-1} and retained 821.4 mAh·g^{-1} at the end of the 90th cycle, representing 81.4% retention of its initial capacity. In contrast, the S_8/MWCNT cathode exhibited significantly inferior electrochemical performance compared to the $S_{70}DMA_{30}Z_5$/MWCNT. Initial cycling at 0.2C yielded a discharge capacity of 706.4 mAh·g^{-1}, which rapidly decayed to 656.47 mAh·g^{-1} after merely 10 cycles. This precipitous decline suggests severe polysulfide shuttling and irreversible loss of active material. When subjected to progressively higher current densities (0.5C, 1C, and 2C), the cathode delivered diminishing reversible capacities of 556, 458.6, 365.7, and 236.3 mAh·g^{-1}, respectively. Most notably, upon returning to 0.2C after extended cycling, the cathode retained only 333.2 mAh·g^{-1}, a mere 47.1% retention of its initial capacity after 90 cycles.

The $S_{70}DMA_{30}Z_5$/MWCNT cells were further examined using the galvanostatic intermittent titration technique (GITT) at a current rate of 0.4 mA·g^{-1} and the corresponding voltage profile is represented in **Fig. 13A**. The results indicate that the $S_{70}DMA_{30}Z_5$/MWCNT cell exhibited a minimal internal resistance (iR) drop of 0.033 V upon discharge and 0.032 V upon charging. Polarization during electrochemical operation manifests as an internal resistance, which can be quantified using **Equation 1**.[36]

$$\Delta R_{internal}\,(\Omega) = |\Delta V_{QCOV-OCV}|/I_a \qquad \textbf{(1)}$$

In this equation, ΔV represents the voltage difference between the quasi-open-circuit voltage (QOCV) and the closed-circuit voltage (CCV), and I_a is the applied current. The $\Delta R_{internal}$ of the cell was found to be 82.5 Ω during discharging and 80 Ω during charging corresponding to very low iR drop of 0.03 V during discharging and 0.02 V during charging processes, respectively [67].

The $S_{70}DMA_{30}Z_5$/MWCNT cells were further characterized by electrochemical impedance spectroscopy (EIS) at 100% state of charge (SOC) after the 1st and 100th cycles, following cycling at a current density of 0.1C. As illustrated in **Fig. 13B**, the Nyquist plots exhibit characteristic impedance features. The Nyquist plots were fitted using an equivalent circuit model to quantify the ohmic resistance (R_e), the solid-electrolyte interface (SEI) resistance (R_{SEI}), and the charge transfer resistance (R_{ct}).

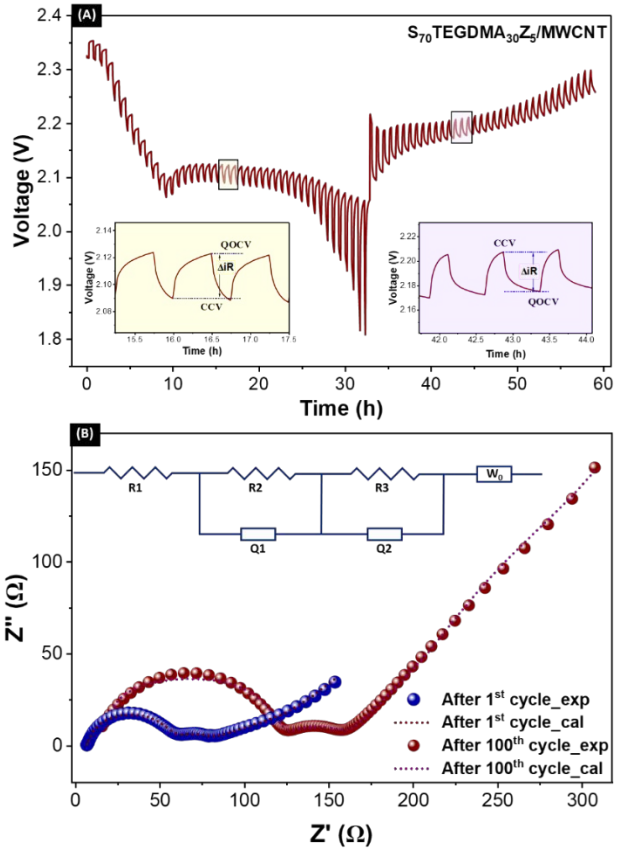

Fig. 13. (A) GITT plot of the $S_{70}DMA_{30}Z_5$/MWCNT-based cell. (B) experimental EIS Nyquist plot and the corresponding fit of the spectrum for $S_{70}DMA_{30}Z_5$/MWCNT-based cell. The inset represents the proposed equivalent circuit model for the corresponding cell

In the equivalent circuit diagram, electrolyte resistance is represented by R1. R2||Q1 represents the R_{SEI}, which is the resistance and capacitance of the passivation layer formed on the lithium metal anode. R3||Q2 indicates the charge transfer resistance, which is associated with the kinetic processes of the polysulfide redox reactions at the cathode/electrolyte interface. An inclined line which corresponds to the Warburg impedance (Z_W) associated with Li^+ diffusion into the bulk of the cathode. In the Nyquist plot of the prepared cell, the high-frequency semicircle is observed to be larger than the low-frequency semicircle. Such behaviour is commonly reported for Li-S cells at 100% SOC [68]. The R_e, R_{SEI}, and R_{ct} of the cell after

View Article Online
DOI: 10.1039/D6CY00375H

1st cycle were found to be 6.7, 53.1, and 19.7 Ω, and they increased to 17.9, 123.7, and 35.5 Ω after 100 cycles. The total resistance of the cell increased from 79.5 to 176.5 Ω at the end of 100 cycles. The increase in resistance is likely attributable to the dissolution of some fractions of organo-polysulfide intermediates into the electrolyte, followed by their migration and irreversible deposition as insulating layers on both the cathode and the lithium metal anode. The change in impedance properties in organo-polysulfidic electrodes might have caused by the changes of copolymer composition or the copolymer distribution in the electrodes, which indicates an area to work further to quantify the changes in organically bound sulfur.

4. Conclusions

Polysulfidic copolymers bearing flexible oligoethylene moieties were synthesized via catalytic inverse vulcanization of sulfur and triethyleneglycol dimethacrylate, using zinc diethyldithiocarbamate, often used as vulcanization accelerators. The successful copolymerization between sulfur and TEGDMA was confirmed using FT-IR, Raman, XPS, XRD, DSC, and TGA analyses. Theoretical DFT studies further revealed that ZDEC facilitates sulfur activation by stabilizing reactive open-shell sulfur species and lowering the energy barrier for radical-mediated C–S bond formation with TEGDMA. The copolymer is used as a cathode active material in Li-S batteries. The use of ZDEC found to be electrochemically inert within the potential window of Li-S batteries, their minor presence after synthesis may be ignored if present in traces. The electrode was fabricated using MWCNTs as a conductive carbon host to accommodate active material within the inter-tubular spaces of the MWCNT structure. Morphological analysis of the composite electrode material was performed using SEM and TEM, revealing an optimally homogeneous electrode structure. EDAX analysis of the copolymer confirmed a sulfur-rich polymer with uniformly distributed oxygen on the surface of the electrode. Electrochemical benchmarking of the fabricated electrode was conducted by assembling it into a CR-2032-type coin cell. The cathode delivered substantially improved initial capacity of 1182.2 $mAh.g^{-1}$ when cycled at a current density of 0.1C. This points to the high active material utilization in the cathode. The cathode demonstrated good capacity retention after 100 charge/discharge cycles, and superior rate capability relative to conventional sulfur-based cathodes. The capacity fading was noted even in the copolymer-based electrode although in a slower rate compared to melt-mixed composites, but the rate performance found to be highly promising, which signifies the stability of such sulfur-based polymeric electrodes even after multiple current density alterations.

Author contributions

Aby Alex: Original draft preparation, investigation, formal analysis, and data curation. Soumyashree Das Adhikari and Hemant Kumar: DFT calculations, data analysis, and interpretation of computational results. Soumyadip Choudhury: Review & editing, supervision, and funding acquisition.

Conflicts of interest

The authors declare no conflict of interest

Data availability

The data supporting this article have been included as part of the Supplementary Information. Supplementary information: Figure S1, S2, S3, S4, S5, S6, S7, S8, S9 & Table S1, S2, S3 and further experimental details. See DOI: https://doi.org/DOI

Acknowledgements

A. Alex acknowledges the Indian Institute of Technology Kharagpur for the institute's doctoral fellowship. S. Choudhury acknowledges the financial support from Anusandhan National Research Foundation (ANRF, erstwhile SERB) – Start-up research grant (Grant Number: SRG/2021/00181) for financial support. S. Choudhury also acknowledges the Indian Institute of Technology Kharagpur for the start-up research grant (ISIRD). All authors acknowledge Prof. Nikhil Kumar Singha for supporting this work.

References

1 H. Raza, S. Bai, J. Cheng, S. Majumder, H. Zhu, Q. Liu, G. Zheng, X. Li and G. Chen, *Electrochem. Energy Rev.*, 2023, **6**, 29.
2 M. R. Al Khazraji, J. Wang and S. Wei, *Energy Technol.*, 2023, **11**, 1–21.
3 M. Zhao, H.-J. Peng, B.-Q. Li and J.-Q. Huang, *Acc. Chem. Res.*, 2024, **57**, 545–557.
4 K. Zhang, Z. Zhao, H. Chen, Y. Pan, B. Niu, D. Long and Y. Zhang, *Small*, 2025, **21**, 1–38.
5 A. Ghorai, A. Alex, S. P. Balmuchu, S. Banerjee and S. Choudhury, *Current Opinion in Electrochemistry*, 2025, **50**, 101639.
6 A. Manthiram, Y. Fu, S. Chung, C. Zu and Y. Su, *Chem. Rev.*, 2014, **114**, 11751-11787.
7 G. Li, S. Wang, Y. Zhang, M. Li, Z. Chen and J. Lu, *Adv. Mater.*, 2018, **30**, 1–19.
8 A. D. Pathak, E. Cha and W. Choi, *Energy Stor. Mater.*, 2024, **72**, 103711.
9 A. Eftekhari and D. W. Kim, . *Mater. Chem. A*, 2017, **5**, 17734–17776.
10 Y. Hu, J. Pan, Q. Li, Y. Ren, H. Qi, J. Guo, Z. Sun and F. Yan, *ACS Sustain. Chem. Eng.*, 2020, **8**, 11396–11403.
11 H. K. Jing, L. L. Kong, S. Liu, G. R. Li and X. P. Gao, *J. Mater. Chem. A*, 2015, **3**, 12213–12219.
12 J. Mu, S. Liao, L. Shi, B. Su, F. Xu, Z. Guo, H. Li and F. Wei, *Polym. Chem.*, 2024, **22**, 473–499.
13 H. Shin, D. Kim, H. J. Kim, J. Kim, K. Char, C. T. Yavuz and J.

W. Choi, *Chem. Mater.*, 2019, **31**, 7910–7921.
14 T. Zhang, F. Hu, W. Shao, S. Liu, H. Peng, Z. Song, C. Song, N. Li and X. Jian, *ACS Nano*, 2021, **15**, 15027–15038.
15 A. Abdul Razzaq, Y. Yao, R. Shah, P. Qi, L. Miao, M. Chen, X. Zhao, Y. Peng and Z. Deng, *Energy Stor. Mater.*, 2019, **16**, 194–202.
16 M. Li, Y. Wang, S. Sun, Y. Yang, G. Gu and Z. Zhang, *Chem. Eng. J.*, 2022, **429**, 132254.
17 L. Zhou, D. L. Danilov, R. A. Eichel and P. H. L. Notten, *Adv. Energy Mater.*, 2021, **11**, 2001304.
18 É. A. Santos, L. M. S. Barros, A. F. Anna, I. Galantini, J. M. Gonçalves, R. Maciel Filho and H. Zanin, *Chemical Engineering Journal*, 2024, **493**, 152429.
19 Z. Ye, S. Zhai, R. Liu, M. Liu, Y. Xu, C. Li, X. Wang and T. Mei, *Chem. Eng. J.*, 2024, **479**, 147847.
20 I. Gracia, H. Benyoucef, X. Judez, U. Oteo, H. Zhang, C. Li, L. M. Rodriguez-martinez and M. Armand, *J. Power Sources,* 2018, **390**, 148–152.
21 J. Fanous, M. Wegner, J. Grimminger, A. Andresen and M. R. Buchmeiser, *Chem. Mater.*, 2011, **23**, 5024–5028.
22 J. M. Chem, J. Fanous, M. Wegner, J. Grimminger, M. Rolff, M. B. M. Spera and M. R. Buchmeiser, *J. Mater. Chem.*, 2012, **22**, 23240–23245.
23 W. J. Chung, A. G. S. J. J. G. E. T. Hyunsik Yoon, H. J. Ji1, R. S. G. Philip T. Dirlam, B. W. G. J. J. W. Ngoc A.Nguyen, A. Jungjin Park, P. Theato, M. E. Mackay and J. P. Y.-E. S. Kookheon Char, , *Nat. Chem.*, 2013, **5**, 518–524.
24 A. G. Simmonds, J. J. Griebel, J. Park, K. R. Kim, W. J. Chung, V. P. Oleshko, J. Kim, E. T. Kim, R. S. Glass, C. L. Soles, Y. E. Sung, K. Char and J. Pyun, *ACS Macro Lett.*, 2014, **3**, 229–232.
25 K. S. Kang, K. A. Iyer and J. Pyun, *Chem. Eur. J.*, 2022, **28**, 1-7.
26 A. Alex, U. Kalita, T. Bhowmik, N. K. Singha and S. Choudhury, ACS Appl. Mater. Interfaces, 2025, **17**, 30029-30043.
27 A. Alex, N. K. Singha and S. Choudhury, *Curr. Opin. Electrochem.*, 2023, **39**, 101271.
28 S. Park, M. Chung, A. Lamprou, K. Seidel, S. Song, C. Schade, J. Lim and K. Char, *Chem. Sci.*, 2022, **13**, 566–572.
29 D. R. Deng, F. Xue, Y. J. Jia, J. C. Ye, C. D. Bai, M. Sen Zheng and Q. F. Dong, *ACS Nano*, 2017, **11**, 6031–6039.
30 J. Kuwabara, K. Oi, M. M. Watanabe, T. Fukuda and T. Kanbara *ACS Appl. Polym. Mater.*, 2020, **2**, 5173–5178.
31 A. Shaan, M. Ghumman, R. Shamsuddin, M. Mahmoud, W. Zaireen, N. Yahya, A. Abbasi and H. Almohamadi, *Sci. Total Environ.*, 2022, **846**, 157417.
32 C. Miao, X. Xun, L. J. Dodd, S. Niu, H. Wang, P. Yan, X. C. Wang, J. Li, X. Wu, T. Hasell and Z. J. Quan, *ACS Appl. Polym. Mater.*, 2022, **4**, 4901–4911.
33 L. Zhao, F. Qiu, X. Deng, Y. Huang, Y. Li, C. Zhao, W. Ren, C. Zou, X. Li, M. Wang and Y. Lin, *ACS Appl. Energy Mater.*, 2022, **5**, 7617-7626.
34 S. Yeşilot, S. Küçükköylü, T. Mutlu, E. Demir and R. Demir-Cakan, *Mater. Chem. Phys.*, 2022, **285**, 126168.
35 A. Rafie, A. Singh and V. Kalra, *Electrochim. Acta*, 2021, **365**, 137088.
36 S. Choudhury, M. Akef, A. Seifert, M. Göbel, M. Gruschwitz, R. Matsidik, C. Tegenkamp and M. Sommer, *ACS Appl. Mater. Interfaces.*, 2023, **16**, 6301–6314.
37 V. K. Tiwari, H. Song, Y. Oh and Y. Jeong, *Energy*, 2020, **195**, 117034.
38 F. Zhao, Y. Li and W. Feng, *Small Methods*, 2018, **2**, 1–34.
39 R. Kiani, D. Sebastiani and P. Partovi-Azar, *ChemPhysChem*, 2022, **23**, 2–6.
40 X. Wu, J. A. Smith, S. Petcher, B. Zhang, D. J. Parker, J. M. Griffin and T. Hasell, *Nat. Commun., 2019, 10, 10035–10044*.
41 L. J. Dodd, Ö. Omar, X. Wu and T. Hasell, *ACS Catal.*, 2021, **11**, 4441–4455.
42 Z. Li, Y. Lu, P. Chen, Q. Zeng, X. Wen, W. Wen, Y. Liu, A. Chen, Z. Li, Z. Wang and L. Zhang, *Electrochim. Acta.*, 2021, **394**, 1–10.
43 H. Wang, B. Zhang, R. Dop, P. Yan, A. R. Neale, L. J. Hardwick and T. Hasell, *J. Power Sources*, 2022, **545**, 231921.
44 M. J. Frisch et al., Gaussian 16, Revision B.01, Gaussian Inc Wallingford CT (2016).
45 R. R. Schmidt, *Angew. Chem. inrernat.*, 1973, **12**, 212–224.
46 R. Steudel, *Top. Curr. Chem.*, 2003, **230**, 81–116.
47 E. Cho, S. M. Pratik, J. Pyun, V. Coropceanu and J. L. Brédas, *ACS Mater. Lett.*, 2022, **4**, 2362–2367.
48 S. J. Kennedy and J. C. Wheeler, *J. Phys. Chem.*, 1983, **87**, 3961–3966.
49 P. B. R. O. Jones, *J. Chem. Phys.*, 2003, **118**, 9257–9265.
50 D. Dondi, A. Buttafava, A. Zeffiro, C. Palamini, A. Lostritto and L. Giannini, *Eur. Polym. J.*, 2015, **62**, 222–235.
51 M. Mousavi, K. Hou, M. Kazemi, C. Li and E. H. Fini, *Adv. Sustain. Syst. 2024,* 2024, **2400322**, 1–11.
52 B. Zhang, H. Gao, P. Yan, S. Petcher and T. Hasell, *Mater. Chem. Front.*, 2020, **4**, 669–675.
53 J. Bao, K. P. Martin, E. Cho, K. S. Kang, R. S. Glass, V. Coropceanu, J. L. Bredas, W. O. N. Parker, J. T. Njardarson and J. Pyun, *J. Am. Chem. Soc.*, 2023, **145**, 12386–12397.
54 J. J. Griebel, R. S. Glass, K. Char and J. Pyun, *Prog. Polym. Sci.*, 2016, **58**, 90–125.
55 D. J. Parker, S. T. Chong and T. Hasell, *RSC Adv.*, 2018, **8**, 27892–27899.
56 L. A. Ko, Y. S. Huang and Y. A. Lin, *ACS Appl. Polym. Mater.*, 2021, **3**, 3363–3372.
57 L. J. Dodd, C. Lima, D. Costa-Milan, A. R. Neale, B. Saunders, B. Zhang, A. Sarua, R. Goodacre, L. J. Hardwick, M. Kuball and T. Hasell, *Polym. Chem.*, 2023, **14**, 1369–1386.
58 P. Bazylewski, R. Divigalpitiya and G. Fanchini, *RSC Adv.*, 2017, **7**, 2964–2970.
59 Z. Ren, X. Jiang, L. Liu, C. Yin, S. Wang and X. Yang, *J. Mol. Liq.*, 2021, **328**, 115437.
60 H. S. Rathore, G. Varshney, S. C. Mojumdar and M. T. Saleh, *J. Therm. Anal. Calorim.*, 2007, **90**, 681–686.
61 J. J. Dale, S. Petcher and T. Hasell, 2022, 6–10.
62 A. Rafie, R. Pereira, A. A. Shamsabadi and V. Kalra, *J. Phys. Chem. C*, 2022, **126**, 12327–12338.
63 M. Waqas, A. Manzoor Soomro, S. Ali, S. Kumar, S. Chan, K. Hussain, F. Hussain Memon and S. Ahmed Shaikh, *ChemistrySelect*, 2020, **5**, 12009–12019.
64 G. Wang, Q. Jiao, Z. Zhang, Y. Zhao, C. Lin, X. Zhang, H. Ma, S. Dai and T. Xu, *Chem. Eng. J. Adv.*, 2021, **8**, 100145.
65 T. C. Chan and S. H. Chung, *ACS Sustain. Chem. Eng.*, 2024, **12**, 14230–14238.
66 H. C. Huang, Y. Y. Chen and Y. A. Lin, *ACS Appl. Energy Mater.*, 2025, **8**, 4618–4628.
67 Q. Zhou, L. Tan, T. Lv, M. Li, J. Zhang, Z. Zhao, X. Jin, Z. Liu, P. Hou, Z. Zeng, S. Deng and G. Dai, *ACS Appl. Mater.*

Interfaces, 2023, **15**, 3037–3046.
68 A. Kilic and D. Eroglu, *ChemElectroChem*, 2021, **8**, 963–971.

View Article Online
DOI: 10.1039/D6CY00235H

View Article Online
DOI: 10.1039/D6CY00235H

Data availability statement

The data supporting this article have been included as part of the Supplementary Information.

Supplementary information: Figure S1, S2, S3, S4, S5, S6, S7, S8, S9 & Table S1, S2, S3 and further experimental details. See DOI: https://doi.org/DOI